

# A Stochastic Conservative Field Transfer Method for Black-box Multiscale and Multiphysics Coupling

Abhiyan Paudel<sup>a</sup>, Cameron W. Smith<sup>b</sup>, Jacob S. Merson<sup>a,b,\*</sup>

<sup>a</sup>*Department of Mechanical, Aerospace, and Nuclear Engineering, Rensselaer Polytechnic Institute, 110 8th St., Troy, NY, 12180, USA*

<sup>b</sup>*Scientific Computation Research Center, Rensselaer Polytechnic Institute, 110 8th St., Troy, NY, 12180, USA*

---

## Abstract

This paper introduces a new method for performing field transfer operations in black-box coupling, when source discretization information is not available. This approach uses a stochastic approximation of the Galerkin projection which leads to a method that asymptotically provides conservation. Error in the accuracy and conservation has been compared to the mesh intersection method and radial basis functions on a simple domain, as well as on meshes of the LTX fusion reactor. For all cases tested, our new method provides higher accuracy and less conservation error than radial basis functions and can be used for black-box coupling, unlike the mesh-intersection method. Additionally, we demonstrate the implementation and performance of our method on an NVIDIA A100 GPU, showing that the cost is competitive with the mesh intersection method.

*Keywords:* multiphysics, coupling, field transfer, unstructured mesh, HPC

---

## 1. Introduction

Transferring field data between disparate discretizations is a critical component of multiscale and multiphysics workflows [1] such as Fluid Structure Interactions (FSI) [2, 3], the Arbitrary Lagrangian-Eulerian (ALE) formulation [4], and mesh adaptation [5]. It has also been observed that there are stability and accuracy benefits to preserving physical constraints such as

---

\*Corresponding author  
*E-mail address:* merso2@rpi.edu

conservation of mass, energy, and momentum while performing field transfers [2, 6, 7]. Many commonly used field transfer techniques, such as interpolation, radial basis functions, and projections based on integrals over source or target elements, rely solely on pointwise field evaluations but generally fail to conserve integral quantities, such as mass or energy [8, 9]. In contrast, mesh intersection or supermesh-based methods provide high-fidelity conservative transfer but require explicit access to full source and target discretizations, limiting their applicability in black-box workflows [6, 8, 9, 10]. The need for black-box coupling arises naturally in workflows that seek to couple machine-learned surrogate models, which typically do not expose a traditional discretization, as well as in multiscale and multiphysics coupling frameworks.

The present work introduces a new strategy for performing projection-based conservative remapping relying only on point-wise field queries while maintaining similar levels of accuracy and conservation to mesh intersection methods. To accomplish this, we utilize a Monte Carlo integration strategy that can avoid the assumptions of continuity that drive the use of mesh intersections. This work was inspired by our recent efforts to support unstructured mesh tallies for neutronics simulations [11, 12].

This work enables conservative multiscale and multiphysics coupling in black-box coupling scenarios when source mesh topology is not available. Furthermore, it is easy to implement and can be used naturally on GPUs or other data-parallel systems. To place our method in the context of the literature, the remainder of this section provides a brief review of related field mapping methods.

Field remapping techniques can largely be categorized into those that carry out pointwise evaluations (e.g., nearest neighbor, or evaluating FEM interpolating polynomials), local reconstruction methods (e.g., radial basis functions or patch-based recovery), and variational methods such as the mesh intersection or supermesh methods. Pointwise evaluation methods are commonly deployed because the only additional component needed for coupling is point localization routines that can map global coordinates to local ones [13, 14, 15].

One of the main advantages of pointwise evaluation methods is that they are often computationally inexpensive. For example, in a finite element library field evaluation is a standard operation that is routinely the focus of optimization. The main cost associated with direct pointwise evaluation is point localization, however if there is infrequent mesh adaptation, this cost

can be amortized over coupling iterations. Additional advantages include that knowledge of the source discretization is only needed for localization and many applications provide APIs to perform evaluations based on global coordinates. A disadvantage of evaluation methods is that they do not provide a mechanism for preserving constraints, such as integral conservation [6, 9].

Local fitting methods such as radial basis functions and patch recovery methods have also found wide adoption for multiphysics coupling and error estimation [13, 16, 17, 18]. The main advantages of these methods is that they can be used in a black-box scenario. Additionally, these methods can be effectively parallelized on GPUs [19, 20, 21], and can be used to provide a global conservation through the introduction of a linear polynomial [2, 13]. In many problems of interest these local fitting methods require parameter tuning to obtain reasonable levels of accuracy and conservation.

Mesh intersection methods were introduced by Jiao and Heath in [8] where they demonstrate a significant advantage when performing Galerkin projections over a common intersected mesh rather than over the source or target discretizations. The use of an intersected mesh removes approximation errors that arise from evaluating the integral of discontinuous functions with standard numerical integration schemes. These methods have been widely extended to efficiently support volume coupling [9, 10] of unstructured meshes, polyhedral meshes, and curved meshes [22]. Given the need for both the source and target discretization information, their applicability in black-box coupling is limited. Likewise, the complexity of the intersection operations complicates GPU execution, and extending the methods to high-dimensional settings is prohibitive.

Key innovations described in this article include

- Formulation of a conservative field transfer operator for multiscale and multiphysics coupling when only pointwise evaluation is available.
- Stochastic approximation of Galerkin projection with quantified conservation behavior.
- Comparison with mesh-intersection and interpolation-based field transfer methods.
- GPU-based implementation and performance characterization of mesh-intersection.

This paper is organized as follows: Section 2 provides background on the Galerkin projection method. Section 3 describes our implementation of the mesh intersection algorithm. Section 4 gives an overview of our novel strategy for conservative coupling without source discretization information. Section 5 provides a set of computational experiments that describe the accuracy, conservation, and efficiency of our new method compared to the mesh intersection and radial basis function methods. Lastly, section 6 provides concluding remarks and future work.

## 2. Conservative Galerkin Projection

Let  $\Omega \subset \mathbb{R}^d$  denote the physical domain of interest, where  $d$  can be any dimension. We assume that the target discretization is a finite element mesh  $\mathcal{M}_t$  with associated FE space  $\mathcal{V}_t = \mathcal{V}(\mathcal{M}_t) = \text{span}\{\psi_i\}_{i=1}^{\mathcal{N}_t} \subset L^2(\Omega)$ , where  $\mathcal{N}_t$  denotes the number of target degrees of freedom. The target field  $f^t \in \mathcal{V}_t$  is represented as

$$f^t(x) = \sum_{i=1}^{\mathcal{N}_t} f_i^t \psi_i(x), \quad f_i^t \in \mathbb{R}. \quad (1)$$

On the source side, we do not assume a particular discretization. The field  $f^s$  may be provided with discretization information (e.g., a source mesh  $\mathcal{M}_s$ ) or accessed only through pointwise evaluations  $f^s(x)$  for  $x \in \Omega$ . The conservative transfer seeks  $f^t$  that is closest to  $f^s$  in the  $L^2$  norm:

$$f^t = \arg \min_{f \in \mathcal{V}_t} \|f^s - f\|_{L^2(\Omega)}, \quad (2)$$

where  $\|(\cdot)\|_{L^2(\Omega)}^2 = \int_{\Omega} (\cdot)^2 d\Omega$ . This  $L^2$  minimization is equivalent to the Galerkin projection, obtained by requiring the residual  $f^t - f^s$  to be orthogonal to the target space,

$$\langle f^t - f^s, \psi_k \rangle_{L^2(\Omega)} = 0, \quad k = 1, \dots, \mathcal{N}_t, \quad (3)$$

with the standard inner product  $\langle u, v \rangle_{L^2(\Omega)} = \int_{\Omega} u v d\Omega$ . Substituting the target expansion into Eq. (3) gives

$$\mathbf{M} \mathbf{f}^t = \mathbf{b} \quad (4)$$

where,

$$M_{ki} = \int_{\Omega} \psi_k \psi_i \, d\Omega, \text{ and} \quad (5)$$

$$b_k = \int_{\Omega} f^s \psi_k \, d\Omega. \quad (6)$$

Here,  $\mathbf{M} \in \mathbb{R}^{\mathcal{N}_t \times \mathcal{N}_t}$  is the symmetric positive-definite sparse mass matrix in  $\mathcal{V}_t$ ,  $\mathbf{f}^t = [f_1^t, \dots, f_{\mathcal{N}_t}^t]^T$  are the target coefficients, and  $\mathbf{b}$  contains the projection of the source field to the target basis. The key distinction is that  $\mathbf{M}$  depends only on the target basis products, whereas  $\mathbf{b}$  requires the product of the target basis and source fields. If the constant function  $1 \in \mathcal{V}_t$ , then the conservation follows as

$$\int_{\Omega} f^t \, d\Omega = \int_{\Omega} f^s \, d\Omega. \quad (7)$$

The formulation in Eq. (2)–(7) is general for any dimension  $d$  and provides a conservative and  $L^2$ -optimal mapping from the source field to the target field.

The mass matrix in Eq. (5) involves the integral of the products of the target basis functions, which can be computed exactly on the target grid using Gaussian quadrature [23, 24]. In contrast, assembling the load vector in Eq. (6) requires integrating the product of a target basis function and source field over  $\Omega$ , which is the primary challenge in conservative remapping. Next, we address the evaluation of the load vector using mesh intersections when source discretization information is available (Section 3) and sampling-based estimators in the absence of such information (Section 4).

### 3. Conservative Coupling with Discretization Information

#### 3.1. Intersection-Based Galerkin Projection

Several approaches have been proposed to compute the load vector using either source- or target-based discretization [8]. However, these schemes can fail to simultaneously preserve accuracy and conservation in field transfer on non-matching meshes [14]. This loss arises because integrating on one mesh requires evaluating quantities defined on the other mesh. In a source-based scheme, the target basis functions must be evaluated at source quadrature points, making the integrand piecewise-defined within each source element.

Conversely, integrating on the target mesh requires evaluating the source field at target quadrature points, making it piecewise-defined within each target element. Because standard quadrature rules assume the integrand is sufficiently regular on each integration element, neither approach is suitable for accurately constructing the load vector. This motivates integration over a common refinement or supermesh defined by geometric intersections of source and target elements.

In practice, the load vector is assembled elementwise. Using the target mesh,

$$b_k = \sum_{t \in \mathcal{M}_t} b_k^t, \quad b_k^t = \int_{\Omega_t} f^s(x) \psi_k(x) \, d\Omega. \quad (8)$$

Although an equivalent elementwise assembly can be performed on  $\mathcal{M}_s$ , we perform all integrations and accumulations over target elements  $t \in \mathcal{M}_t$  in this work.

Because  $f^s$  is not regular on a target element  $t$  when the meshes are non-matching, the integral on  $\Omega_t$  must be decomposed into integrals over the geometric intersections of  $t$  with the source elements:

$$\int_{\Omega_t} f^s(x) \psi_k(x) \, d\Omega = \sum_{s \in \mathcal{S}(t)} \int_{\Omega_t \cap \Omega_s} f^s(x) \psi_k(x) \, d\Omega. \quad (9)$$

where  $\mathcal{S}(t) = \{s_i : |\Omega_t \cap \Omega_{s_i}| > 0\}$  denotes the set of source elements that geometrically intersect  $t$ . Therefore, there are two clear challenges in computing the load vector:

1. identifying all nonempty intersections  $t \cap s$  (i.e.,  $\mathcal{S}(t)$ ); and
2. evaluating the integrals over these intersection regions.

The following section provides an overview of our GPU-based implementation of the mesh intersection method.

### 3.2. Common-Refinement/Supermesh Overview

One of the earliest general frameworks for conservative field transfer on non-matching meshes is the *common-refinement* method introduced by Jiao and Heath [8, 25]. Their approach constructs a global intermediate mesh by projecting the points of one surface onto the other and defining all edge intersections. This results in a globally consistent overlay mesh; however, the method is applicable only to 2D surface meshes. Extending such a global

refinement strategy to 3D volume meshes is prohibitively expensive as the required global overlay and intersection computations results in substantial memory usage and computational overhead. Farrell et al. [10] addressed this limitation by introducing the *supermesh* method. The supermesh is defined as a collection of all non-empty intersections:

$$\mathcal{M}_{ts} = \{t \cap s : t \in \mathcal{M}_t, s \in \mathcal{M}_s, |\Omega_t \cap \Omega_s| > 0\}$$

as illustrated in Figure 1. Unlike the global common refinement approach, the supermesh is constructed locally. For each target element, intersecting source elements are identified, and each intersection region  $t \cap s$  is meshed using Eberly’s clipping algorithm [26]. Although this local construction avoids building a global overlay mesh, it still requires forming and storing an explicit mesh for every intersection region, which can become memory-intensive for large problems. Moreover, the implementation in [10] is CPU-based and relies on classical geometric-clipping procedures.

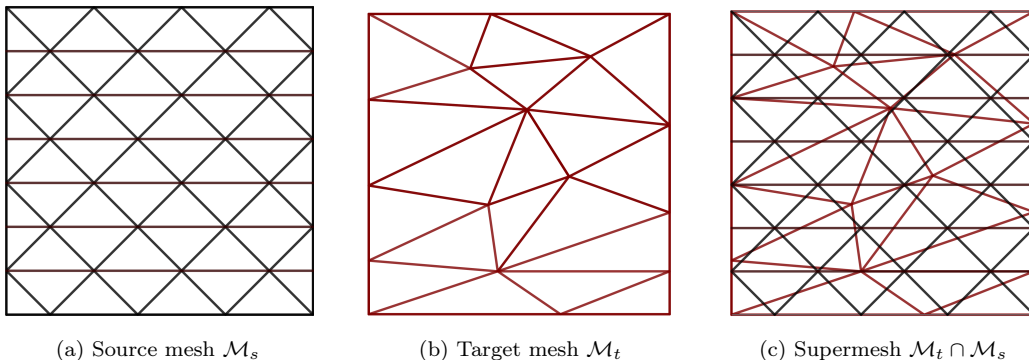


Figure 1: The supermesh (c) is constructed from geometric intersections of source (a) and target (b) elements.

### 3.3. R3D-Based Intersection and GPU Integration

In the current work, the construction of the local supermesh is handled using the R3D algorithm [27, 28] as implemented in the `Omega_h` library [5]. This approach is naturally suited to the GPU execution. Instead of constructing and storing an explicit intersection mesh for every non-empty region  $t \cap s$ , the present method computes all geometric intersections and performs numerical integration *on-the-fly*. R3D represents each clipped region  $t \cap s$  not as a triangulated mesh but as a convex polytope that stores

the number of vertices, their coordinates, and the neighboring vertex lists defining the polygonal face. The next section describes the procedure for identifying intersecting source elements, which serve as inputs to the R3D clipping and integration stages.

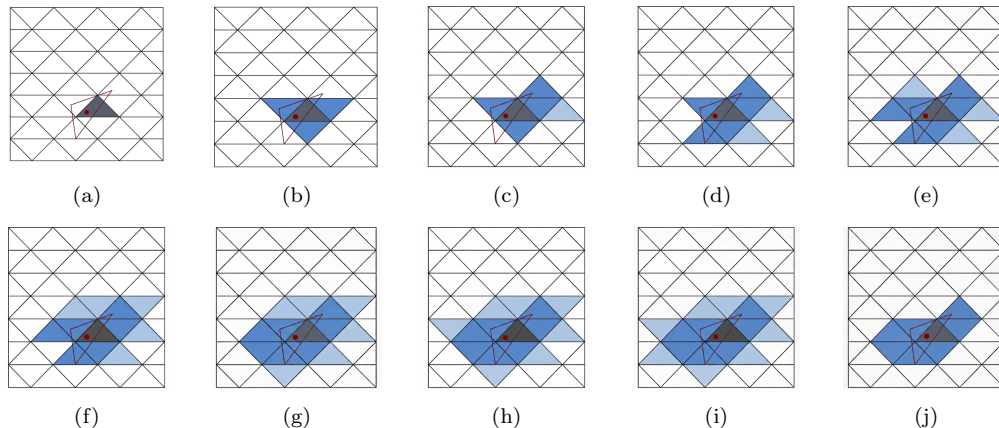


Figure 2: Adjacency-based identification of intersecting source elements for a single target element (red) and its centroid (red dot). Figures (a)–(j) illustrate the progressive expansion of the search front which is expanded from the gray element which is identified through localization of the target element centroid. The dark blue elements represent the expanded set of search elements in each step which constitute the integration regions for the load-vector assembly; light blue elements indicate source elements that are traversed during the search but do not intersect the target element of interest.

### 3.3.1. Adjacency-Based Intersection Search

To construct a local supermesh, the intersecting pair of elements of  $\mathcal{M}_s$  and  $\mathcal{M}_t$  must be identified. The algorithm applied in this study is shown in Figure 2 and summarized below.

1. For a given target element  $t \in \mathcal{M}_t$ , the centroid of  $t$  (depicted with red dot) is mapped onto the source mesh  $\mathcal{M}_s$  through point localization, yielding the initial seed source element  $s_0$  as highlighted in grey color (Figure 2a).
2. A breadth-first traversal of the source-mesh adjacency graph is initiated from  $s_0$ . Each visited source element  $s$  is tested for geometric intersection with  $t$  using R3D [27]. Neighbors of intersecting source elements are added to the search front, while non-intersecting elements are discarded. The search expands until no new neighbors remain to be tested. (Figure 2b–Figure 2i)

3. The output is the set  $\mathcal{S}(t)$  of source elements intersecting  $t$ . The corresponding regions  $t \cap s_i$  form the integration subdomains for load vector assembly (Figure 2j).

The same adjacency-based traversal is performed for every target element  $t \in \mathcal{M}_t$  to identify its intersecting source elements.

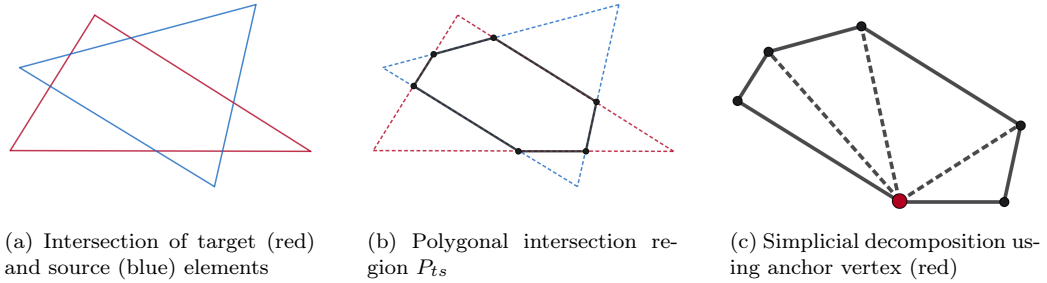


Figure 3: Intersection integration procedure: geometric clipping, polytope construction, and simplicial decomposition for numerical quadrature.

### 3.3.2. Intersection Integration

Once the intersection set is identified for a target element  $t$ , the contribution to the load vector is assembled by integrating over each intersection region  $t \cap s$ . Unlike supermesh-based approaches, no explicit intersection mesh is stored. Instead, each intersection region is generated, decomposed, and used for integration on the fly. The overall procedure is illustrated in Figure 3 and proceeds as follows:

1. For each target element  $t \in \mathcal{M}_t$  processed independently and in parallel on the GPU, initialize its local load vector  $b_k^t$ .
2. For every intersecting source element  $s \in \mathcal{S}(t)$ , compute the geometric intersection  $P_{ts} = t \cap s$  using the R3D clipping algorithm. As shown in Figure 3a, this operation takes the target element (red) and source element (blue) and produces a convex polygon representing their overlap.
3. The resulting intersection region  $P_{ts}$  is represented as a convex polytope via its planar graph, storing only vertex coordinates and adjacency information. Figure 3b illustrates the polygonal intersection region obtained after clipping.

4. The vertices of each polygon of  $P_{ts}$  are sorted into a consistent counter-clockwise (CCW) ordering to enable a stable simplicial decomposition.
5. A simplicial decomposition is then performed on the fly by selecting an anchor vertex (shown in red in Figure 3c) and forming triangles (in 2D) by connecting the anchor to successive vertex pairs.
6. Numerical quadrature is applied on each simplex to accumulate the local contribution to the load vector associated with  $t$ .
7. After all  $s \in \mathcal{S}(t)$  have been processed, the contributions from all simplices of all intersection polytopes  $P_{ts}$  are summed into  $b_k^t$ . The global load vector  $b_k$  is then assembled from the element-local vectors  $b_k^t$ .

This approach is fully local, memory efficient, and naturally suited to GPU parallelism.

## 4. Conservative Coupling without Discretization Information

### 4.1. Monte Carlo Approximation of the Galerkin Projection

In this section, we consider the black-box coupling regime, in which the source discretization information is unavailable and the source field  $f^s(x)$  is accessible only through pointwise evaluations. In this setting, the mass matrix in the Galerkin system Eq. (4) is assembled deterministically on the target mesh, whereas the load vector entries in Eq. (6) must be approximated.

Following the element-wise assembly described in Eq. (8), we approximate each target-element load integral by sampling within  $t$  and assemble the load vector by summing the target-element contributions. Let  $p_t(\mathbf{x})$  be a probability density function on  $t$  such that

$$p_t(\mathbf{x}) \geq 0, \quad \int_{\Omega_t} p_t(\mathbf{x}) d\Omega = 1. \quad (10)$$

Let  $\mathbf{X}_{t,1}, \mathbf{X}_{t,2}, \dots, \mathbf{X}_{t,N}$  be i.i.d. samples drawn from  $p_t(\mathbf{x})$ . The Monte Carlo estimator of the element contribution  $b_k^t = \int_{\Omega_t} f^s(x)\psi_k(x) d\Omega$  is

$$\widehat{b}_k^t = \frac{1}{N} \sum_{i=1}^N \frac{f^s(\mathbf{X}_{t,i}) \psi_k(\mathbf{X}_{t,i})}{p_t(\mathbf{X}_{t,i})}. \quad (11)$$

This estimator for the right-hand side of the Galerkin projection is unbiased since

$$\mathbb{E}[\widehat{b}_k^t] = \int_{\Omega_t} \frac{f^s(x)\psi_k(x)}{p_t(x)} p_t(x) d\Omega = \int_{\Omega_t} f^s(x)\psi_k(x) d\Omega = b_k^t. \quad (12)$$

For uniform sampling within the target element,  $p_t(\mathbf{x}) = 1/|\Omega_t|$  and Eq. (11) reduces to

$$\widehat{b}_k^t = \frac{|\Omega_t|}{N} \sum_{i=1}^N f^s(\mathbf{X}_{t,i}) \psi_k(\mathbf{X}_{t,i}). \quad (13)$$

Because each element-wise estimator  $\widehat{b}_k^t$  is unbiased for  $b_k^t$ , the assembled entry  $\widehat{b}_k = \sum_{t \in \mathcal{M}_t} \widehat{b}_k^t$  is an unbiased estimator of  $b_k$ . Since  $\mathbf{M}$  is deterministic and the randomized coefficient vector  $\widehat{\mathbf{f}}^t = \mathbf{M}^{-1} \widehat{\mathbf{b}}$  satisfies  $\mathbb{E}[\widehat{\mathbf{f}}^t] = \mathbf{f}^t$ , the Monte Carlo Galerkin projection is unbiased in expectation.

The process involved in approximating the Galerkin projection using the Monte Carlo method is summarized below.

1. For each target element  $t \in \mathcal{M}_t$ , initialize the local contribution  $b_k^t$  to the load vector.
2. Choose a sample count  $N$  per element. For  $j = 1, \dots, N$  draw two independent scalars  $\xi_j \sim \text{Uniform}(0, 1)$  and  $\eta_j \sim \text{Uniform}(0, 1)$ , and convert  $(\xi_j, \eta_j)$  to area-uniform barycentric weights on the reference triangle using the mapping in [29]. For efficiency, the same set of parametric coordinates are reused for all elements and element-specific global coordinate locations  $x_j \in t$  are obtained by mapping through the vertices of each  $t$ .
3. Perform point localization to find the source element.
4. For each sample point  $x_j$ , query the source value  $f^s(x_j)$  and evaluate the target basis functions associated with element  $t$  at  $x_j$ .
5. For each basis function  $\psi_i$  supported on  $t$ , calculate the Monte Carlo integral as,

$$\widehat{b}_i^t = \frac{|\Omega_t|}{N} \sum_{j=1}^N f^s(x_j) \psi_i(x_j)$$

6. After all samples are processed, assemble the global load vector  $b_k$  from the element-local contributions  $b_k^t$ , and solve  $\mathbf{M} \mathbf{f}^t = \mathbf{b}$ .

#### 4.2. Sampling Strategies and Integration Error

The choice of sampling method plays a critical role in the accuracy of Monte Carlo-based numerical integration. To study the impact of the sampling methods on the accuracy of the Monte Carlo integration, we consider the integration of a linear function given by

$$f(x, y) = x + y \quad (14)$$

over the domain  $\Omega$  shown in the Figure 5a.

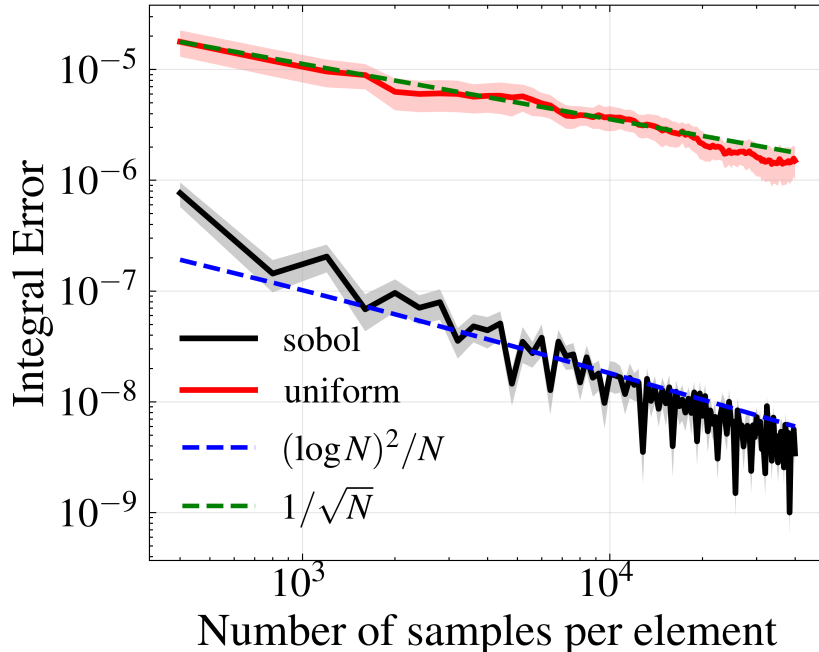


Figure 4: Integral error vs number of samples

In this study, we compare uniform random Monte Carlo (MC) sampling with Sobol-sequence-based quasi-Monte Carlo (QMC) sampling. The sampling is performed as described in the previous section. The number of samples per target element is varied over the range  $400 \leq N \leq 40000$ .

To quantify the integral accuracy, we compute the relative integral error

$$E_{int} = \frac{|I - \hat{I}_N|}{|I|} \quad (15)$$

where  $I$  denotes the exact integral and  $\hat{I}_N$  is the Monte Carlo estimate obtained using  $N$  samples per mesh element.

Figure 4 presents a log-log comparison of the relative integral error as a function of the number of samples per element for uniform random Monte Carlo sampling and Sobol-based quasi-Monte Carlo sampling. For uniform random sampling, the error decays at the expected rate of  $\mathcal{O}(N^{-1/2})$ , closely following the theoretical reference curve shown as a green dashed line. In

contrast, Sobol sampling achieves significantly lower error across all sample counts, with an observed convergence rate consistent with the  $\mathcal{O}((\log N)^2/N)$  behavior characteristic of QMC methods.

Across the full range of samples, Sobol sampling yields approximately one to two orders of magnitude smaller error than uniform random sampling. The shaded bands indicate the variability across 30 independent realizations, which decreases as the number of samples increases, demonstrating the improved robustness of both estimators at larger  $N$ . These results confirm the theoretical advantages of low-discrepancy sequences for numerical integration [30] and motivate the use of Sobol-based sampling in the Monte Carlo field-transfer studies presented in the subsequent sections.

## 5. Numerical Comparison

In the present work, our objective is to compare the accuracy, conservation and performance properties of three field-transfer techniques:

1. a non-conservative Radial Basis Function (RBF)-based method,
2. a deterministic, conservative Mesh-Intersection (MI)-based method, and
3. an asymptotically conservative Monte Carlo (MC)-based method.

All three methods transfer a scalar field from one mesh to a non-matching mesh on a shared geometric domain.

The RBF method used here is a local weighted polynomial fitting method. The corresponding minimization problem is stated as

$$\min_c \|\phi \cdot (Ac - b)\|_2^2 + \lambda \|c\|_2^2, \quad (16)$$

where  $A$  is the Vandermonde matrix constructed from the set source points within a radius  $r$  of the target point,  $\phi$  is the diagonal weight matrix,  $\lambda$  is the regularization parameter,  $b$  is the vector of source field values. All presented tests use the C4 basis function. The complete details of the C4 basis function and source set construction are described in [31]. For this work, we expand the radius so that each target element has at least the minimum number of source supports required for linear fitting.

### 5.1. Convergence Analysis

An important property of supermesh-based Galerkin projection, as highlighted by Farrell and Maddison [10], is that the projection error can be evaluated exactly up to quadrature (and roundoff) on the supermesh. Since each intersection region forms a geometric subdomain on which both the source and target finite element spaces are exactly representable, the error field

$$g = f^s - f^t \quad (17)$$

is itself a well-defined function on every cell of the supermesh. This enables the exact evaluation of the error by integrating  $g$  over  $\mathcal{M}_{ts}$  in any desired norm. To quantify the quality of the field transfer, we evaluate the two relative integral norms that measure accuracy and global conservation.

*Continuous (supermesh-based) accuracy error.* The relative  $L^2(\Omega)$  accuracy error, evaluated using the supermesh-based integration, is defined as:

$$E_{L^2} = \frac{\|f^s - f^t\|_{L^2(\Omega)}}{\|f^s\|_{L^2(\Omega)}} = \frac{\left(\int_{\Omega} (f^s(x) - f^t(x))^2 \, d\Omega\right)^{1/2}}{\left(\int_{\Omega} (f^s(x))^2 \, d\Omega\right)^{1/2}} \quad (18)$$

*Continuous (supermesh-based) conservation error.* To examine how well the global integral of the field is preserved, we use the relative conservation (mass) error evaluated on the supermesh:

$$E_{\text{mass}}^{\text{SM}} = \frac{\left|\int_{\Omega} f^s(x) \, d\Omega - \int_{\Omega} f^t(x) \, d\Omega\right|}{\left|\int_{\Omega} f^s(x) \, d\Omega\right|}. \quad (19)$$

For this study, we generated the sequence of target/source mesh pairs with progressively smaller characteristic mesh size  $h$  using gmsh [32]. The target/source meshes are topologically different even though their characteristic sizes match at each refinement level, as used in supermesh-based convergence studies in [10]. The field transfer is computed from source to target space for these meshes and both error metrics are evaluated and recorded. All fields utilize linear ( $p = 1$ ) Lagrange shape functions.

For the Monte Carlo integration, each target element is sampled with Sobol sequence points mapped to uniformly distributed barycentric coordinates within the triangle as discussed in the previous section. To assess the

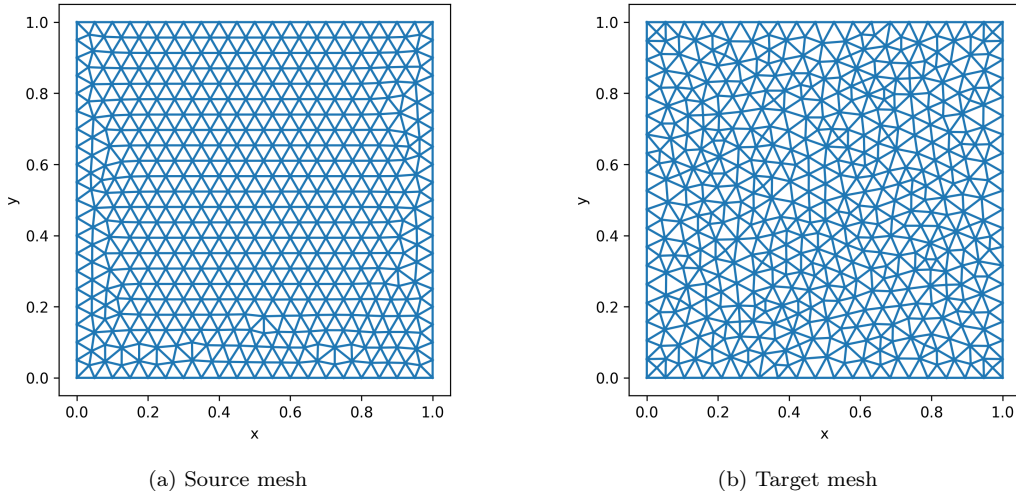


Figure 5: Representative source and target meshes used in the performance analysis

effect of sampling density on accuracy and conservation, we evaluate a range of samples per target element,  $N$ , with  $N \in \{400, 800, 1200, 1600\}$ . These values are held constant across refinement levels to isolate the influence of mesh size  $h$  from that of sampling density. The function used for all tests is the smooth scalar field

$$f(x, y) = \sin(x) \cos(y) + 2. \quad (20)$$

The resulting accuracy and conservation errors obtained from the MI, MC and RBF methods are shown in Figure 6.

In Figure 6a, the MI approach exhibits a convergence rate close to  $\mathcal{O}(h^2)$ , consistent with the expected behavior for linear finite elements and matching the observations of Farrell and Maddison [10]. The Monte Carlo results show the expected dependence on sampling density. For 400–1200 samples, the accuracy reaches a plateau as the mesh size is reduced, whereas  $N = 1600$  samples produce errors comparable to the mesh-intersection method. This indicates that, for Monte Carlo integration, the sample count must increase as the mesh is refined to maintain accuracy. On the other hand, the RBF based method performs worse across all refinement levels as compared to MI and MC approaches.

The conservation results in Figure 6b show that the MI and MC achieve errors on the order of  $10^{-6}$ – $10^{-7}$ . For the MC, the conservation error decreases with both mesh refinement and increased sample count, consistent

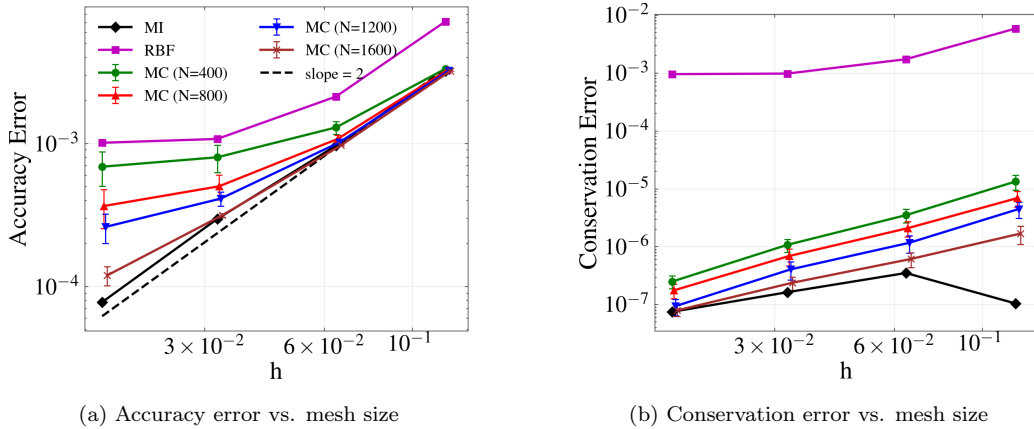
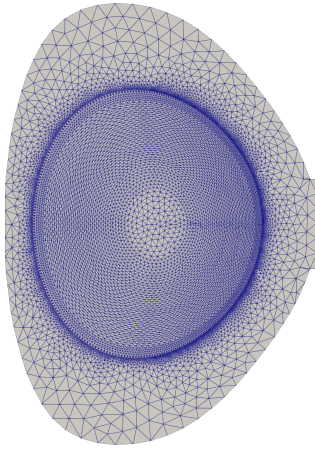


Figure 6: Convergence of accuracy and conservation errors with mesh refinement.

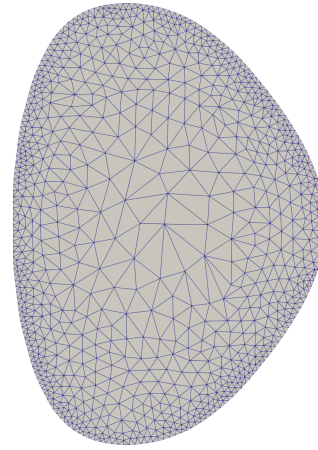
with the statistical convergence of Monte Carlo integration. With sufficiently large  $N$ , MC approaches the conservation performance of the MI technique. As expected, the RBF based field transfer method exhibits conservation errors several orders of magnitude larger for all element sizes, since it does not preserve integral quantities by construction.

### 5.2. Iterative Analysis

This numerical experiment examines the long-term behavior of each transfer operator under repeated remapping. We initiate from a reference field on the first mesh and apply a round-trip map (first mesh  $\rightarrow$  second mesh  $\rightarrow$  first mesh) for a prescribed number of iterations without introducing any additional modifications to the field. After each round-trip, both the accuracy and conservation errors are evaluated on the first mesh relative to the initial (reference) field values. This analysis provides insight into whether repeated application of a transfer operator introduces accumulating errors in the solution and/or integral quantities. Unlike the convergence study, which evaluates continuous norms using supermesh integration, the metrics below are computed on the first mesh: accuracy is measured in the discrete  $\ell^2$  norm of the degrees of freedom, and conservation is evaluated by quadrature of the reconstructed field on the first mesh.



(a) Mesh with 20319 elements of the LTX reactor used by the XGC code for evolving the plasma profiles.



(b) Mesh with 1784 elements of the LTX reactor used by the DEGAS2 code to evolve the neutral particle profiles.

Figure 7: Meshes of the LTX reactor

*Discrete (DoF-based) accuracy error.* The relative  $\ell^2$  accuracy error is computed as

$$E_{\ell^2} = \frac{\|f^{\text{approx}} - f^{\text{ref}}\|_2}{\|f^{\text{ref}}\|_2} = \frac{\left(\sum_{i=1}^{\mathcal{N}} (f_i^{\text{approx}} - f_i^{\text{ref}})^2\right)^{1/2}}{\left(\sum_{i=1}^{\mathcal{N}} (f_i^{\text{ref}})^2\right)^{1/2}}, \quad (21)$$

where  $\mathcal{N}$  is the total number of degrees of freedom (control points) on the first mesh,  $f^{\text{ref}}$  denotes the initial (reference) DoF values, and  $f^{\text{approx}}$  denotes the DoF values after a given number of round-trip iterations.

*Discrete (mesh-based) conservation error.* The relative conservation (mass) error is computed as

$$E_{\text{mass}}^{\text{M1}} = \frac{\left|\int_{\Omega} f^{\text{approx}}(x) \, d\Omega - \int_{\Omega} f^{\text{ref}}(x) \, d\Omega\right|}{\left|\int_{\Omega} f^{\text{ref}}(x) \, d\Omega\right|}, \quad (22)$$

where, the integrals are evaluated using a quadrature rule on the first mesh.

For this study we use the LTX reactor configuration, where the reference field as given in Eq. 20 is defined on the XGC mesh (Figure 7a) and repeated mapping is performed through the DEGAS2 mesh (Figure 7b). For the MC-based transfer, we compare several sampling levels  $N \in \{400, 800, 1200, 1600\}$

samples per target element, consistent with the sampling-density used in the convergence study. Figures 8a and 8b depict the evolution of accuracy

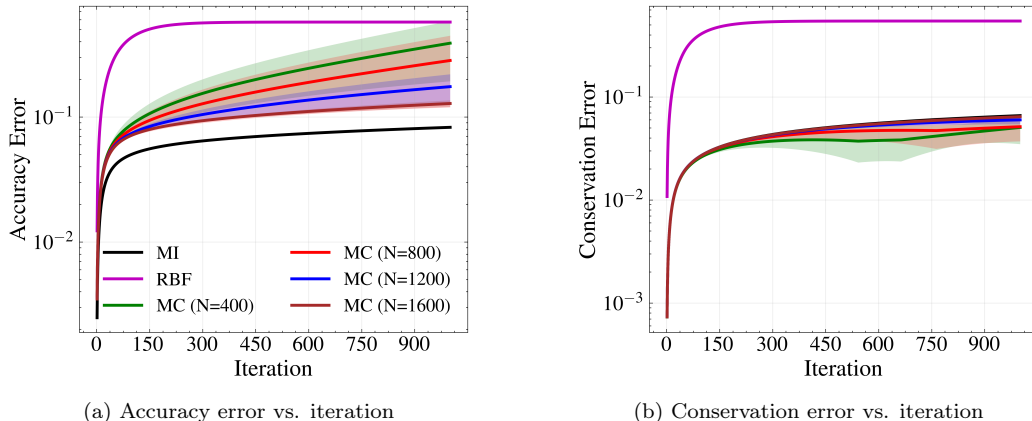


Figure 8: Evolution of accuracy and conservation errors with iteration.

and conservation errors with iteration. In both metrics, all methods exhibit a rapid rise in error over the first few iterations, which is followed by a much slower growth that approaches a nearly steady level over high iteration counts.

From Figure 8a, the deterministic mesh-intersection (MI) method consistently yields the smallest accuracy error and the most stable long-iteration behavior. The Monte Carlo (MC) results display a clear dependence on the number of samples per target element such that the accuracy error decreases monotonically as  $N$  increases. In particular, the  $N = 400$  case deviates the most from MI and continues to separate as the iteration count grows, while  $N = 1600$  closely follows the MI curve throughout the entire iteration range. The shaded bands show that MC variability is widest for small  $N$  and shrink as  $N$  increases, confirming improved repeatability at higher sampling densities.

In contrast, the conservation behavior in Figure 8b shows that MI and all MC sampling levels remain within a comparable range (same order of magnitude) over the full iteration counts, with only modest differences between  $N = 400$  and  $N = 1600$ . The dependence of conservation error on sampling density is much weaker than for the accuracy metric. This suggests that, in this problem, global integral errors are less sensitive to sampling density than fieldwise  $\ell^2$  errors under repeated remapping. The MC uncertainty

bands again decrease with  $N$ , indicating reduced statistical variability for larger sample counts.

The RBF-based transfer performs substantially worse in both plots, as it gives a much larger error level and remains well separated from MI and MC for all iterations. This is consistent with the fact that the RBF approach does not enforce conservation, and repeated application amplifies both fieldwise and integral error. The iterative experiment reinforces the observation made in the convergence study that MC approaches MI behavior at sufficiently large  $N$ .

### 5.3. Performance Analysis

In this section, we examine the scaling properties of the different field transfer methods with respect to the problem size. The sequence of meshes are created with the number of elements ranging from 1000 to 2.3 million using gmsh [32]. An example of the meshes used for this study are shown in Figure 5.

For the mesh–intersection (MI) method, the dominant costs are: (i) the adjacency-based search used to identify intersecting source elements for each target element, (ii) R3D clipping to construct the intersection polytopes  $P_{ts}$ , performed during initialization and (iii) on-the-fly simplicial decomposition and numerical integration over these regions, and (iv) a global solve of Equation (4) performed online during each coupling iteration. In contrast, MC avoids geometric operations entirely; its cost is dominated by evaluating (i) localizing the target points in the source mesh during initialization and (ii) evaluating the source field at  $N$  Sobol–barycentric sample points within each target element, and (iii) a global solve of Equation (4) performed online during each coupling iteration. The cost of the RBF method is dominated by (i) a search to find source points around the target point during initialization and (ii) a local polynomial fitting and evaluation routine performed online during each coupling iteration.

The MI and MC methods incur a per-target-element cost, but the nature of the work differs: intersection search, geometric clipping and integration for MI versus repeated point-localization and function evaluation for MC. The RBF method incurs a per node cost.

All the profiling experiments were run on an NVIDIA A100 GPU and the timings reported below correspond to GPU time only. The timings reported in Figures 9a and 9b reflect initialization (setup), and online costs, respectively. Initialization is the cost that must be paid once for each unique mesh

(intersection computation, localization, and source point set identification). Online costs are those that must be paid for each coupling iteration such as evaluation of integrals and global solve for MI and MC and local solve and evaluation for RBF.

For localization, we make use of a uniform grid search implemented in PCMS [31] with the number of grid cells in each direction given by  $nx = ny = \text{int}(L\sqrt{\#\text{elements}})$ , where  $L$  is the characteristic size of the domain. The localization grid size was chosen to balance performance against memory use. The localization method is critical to achieving performance during initialization, however in a black-box coupling scenario, where no source discretization is available, there is limited opportunity to control the localization procedures. Furthermore, some black-box source fields such as machine-learned surrogates may not require explicit global-to-local mapping.

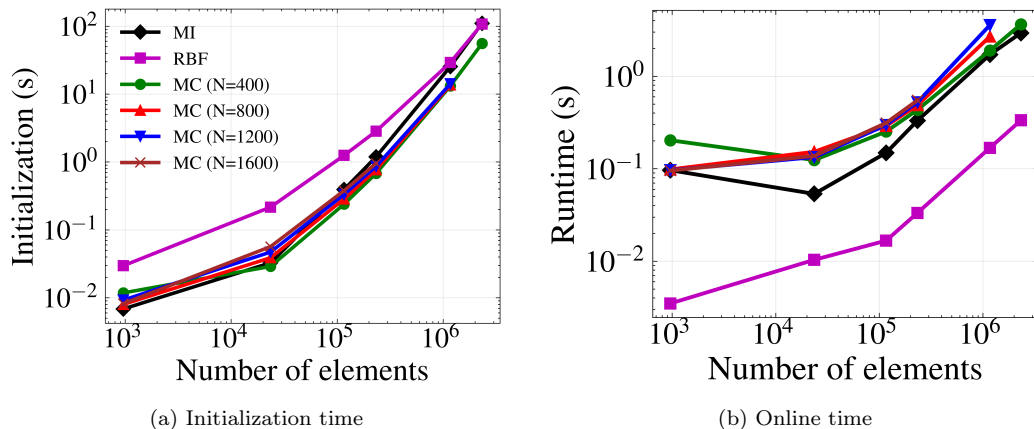


Figure 9: Timing results of performing field transfer using MI, MC, and RBF methods on an NVIDIA A100 GPU for mesh sizes ranging from 1000 elements to 2.3 million elements.

Some of the largest MC cases exceeded available memory on the GPU and are omitted from the plot. Future implementations can mitigate this by performing batching of the point evaluations.

The initialization cost for each method (Figure 9a) scales with the number of elements and number of sample points. The initialization cost for the RBF method is the greatest for all mesh sizes tested due to the iterative method for radius adaptation. Although this increases the initialization cost, minimizing the number of source points reduces the online cost. The initialization cost for the MI and MC cases are similar. The MC results are reported for a

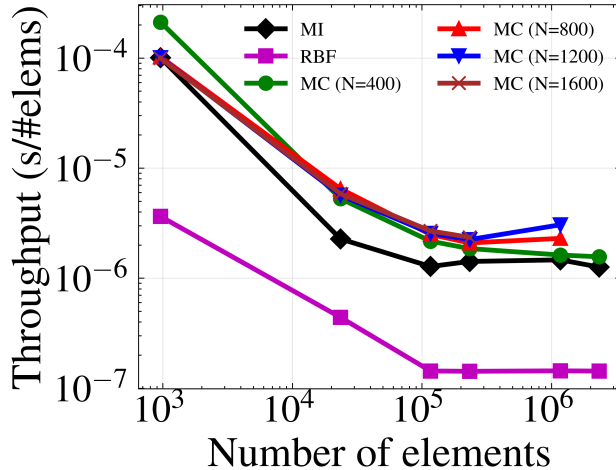


Figure 10: Online cost normalized by number of elements.

single realization as there is minimal variation due to the nearly uniform distribution of target points in the source mesh. Methods such as variance reduction that could reduce the number of sample points needed for the MC cases could make the performance of the MC method faster than the mesh intersection method. Since the initialization only needs to be done once for a pair of fixed meshes, this cost is amortized across coupling steps.

The online cost (Figure 9b) is the cost of performing a single field transfer operation once the initialization is complete. Due to the local nature of the solution methodology, the RBF method incurs the lowest cost for all mesh sizes. For all mesh sizes, the mesh intersection method was faster, but maintained similar linear scaling with the number of elements as the MC method. The online cost of the MC method does not vary across realizations.

The data from Figure 9b is replotted normalized by the number of elements in Figure 10. This shows an initial drop off in the cost per element as the amount of parallel work increases to overcome the latencies associated with launching GPU work and a plateau indicating linear scaling with the number of elements. The onset of the plateau for all three methods starts at around  $10^5$  elements.

## 6. Conclusion

In this paper we introduce a novel method for supporting black-box coupling that does not rely on field regularity but can still provide asymptotic

convergence of integral quantities. Such fields include machine-learned surrogates and other non-standard field representations. Our method has been compared against radial basis functions which are often used in black-box coupling as well as the mesh intersection method which cannot be used in black-box coupling due to the need for full information about the source discretization. In our computational experiments, our new method provides better accuracy and conservation error than the radial basis function approach and converges to the level of accuracy and conservation error of the mesh intersection method as the number of sample points is increased.

We also compare the performance of our new method on the GPU compared with the mesh intersection method and radial basis function method. We find that the radial basis function method is fastest for performing evaluations, and our new method is competitive with the mesh intersection method and likely to improve with further optimization and implementation of variance reduction.

One limitation of our method is that it is non-deterministic since it is a Monte Carlo method. In practice, the user of this method should track the point evaluation variability and integral convergence with the number of points sampled. One promising direction of future work that may accelerate convergence, is the use of variance reduction methods. Another promising direction of future work is to support conservative field transfer of high-dimensional fields, such as the five- and six-dimensional fields that are needed for coupled fusion simulations [31].

## Acknowledgement

This research was supported by the U.S. Department of Energy, Office of Science Office of Advanced Scientific Computing Research, Scientific Discovery through Advanced Computing (SciDAC) Program through multiple grants including the FASTMath SciDAC Institute (DE-SC0021285 & DE-AC52-0TNA27344), and multiple Fusion Energy SciDAC subcontracts including StellFoundry: High-fidelity Digital Models for Fusion Pilot Plant Design (DE-AC02-09CH11466), Computational Evaluation and Design of Actuators for Core-Edge Integration (CEDA) (DE-AC02-09CH11466), Hi-fiStell: High-Fidelity Simulations for Stellarators (DE-SC0024548) and Center for Advanced Simulation of RF - Plasma - Material Interactions (DE-SC0024369). This research is also supported through a DOE Fusion Innovation Research Engine (FIRE) Collaboratives Program through a grant ti-

tled Mitigating Risks from Abrupt Confinement Loss (MIRACL) (DE-AC02-09CH11466). This research is also supported through a DOE ASCR SBIR entitled Geometry and Meshing Technologies to Support Fusion Energy System Simulations (DE-SC0024838). Any opinions, findings, and conclusions or recommendations expressed in this material are those of the author(s) and do not necessarily reflect the views of the U.S. Department of Energy.

### **Declaration of generative AI and AI-assisted technologies in the manuscript preparation process**

During the preparation of this work, the author(s) used ChatGPT (OpenAI) and Perplexity AI to identify and locate relevant academic papers, and Overleaf's research-tailored AI language feedback features for language refinement. After using these tools, the author(s) thoroughly reviewed, verified, and edited all content to ensure accuracy and maintain full responsibility for the integrity and originality of the manuscript.

### **References**

- [1] D. E. Keyes, L. C. McInnes, C. Woodward, W. Gropp, E. Myra, M. Pernice, J. Bell, J. Brown, A. Clo, J. Connors, E. Constantinescu, D. Estep, K. Evans, C. Farhat, A. Hakim, G. Hammond, G. Hansen, J. Hill, T. Isaac, X. Jiao, K. Jordan, D. Kaushik, E. Kaxiras, A. Koniges, K. Lee, A. Lott, Q. Lu, J. Magerlein, R. Maxwell, M. McCourt, M. Mehl, R. Pawlowski, A. P. Randles, D. Reynolds, B. Rivière, U. Rüde, T. Scheibe, J. Shadid, B. Sheehan, M. Shephard, A. Siegel, B. Smith, X. Tang, C. Wilson, B. Wohlmuth, Multiphysics simulations: Challenges and opportunities, *The International Journal of High Performance Computing Applications* 27 (1) (2013) 4–83. doi:10.1177/1094342012468181.  
URL <http://journals.sagepub.com/doi/10.1177/1094342012468181>
- [2] A. de Boer, A. H. van Zuijlen, H. Bijl, Comparison of conservative and consistent approaches for the coupling of non-matching meshes, *Computer Methods in Applied Mechanics and Engineering* 197 (49) (2008) 4284–4297. doi:10.1016/j.cma.2008.05.001.  
URL <https://www.sciencedirect.com/science/article/pii/S0045782508001916>

- [3] R. K. Jaiman, X. Jiao, P. H. Geubelle, E. Loth, Assessment of conservative load transfer for fluid-solid interface with non-matching meshes, *International Journal for Numerical Methods in Engineering* 64 (15) (2005) 2014–2038. doi:10.1002/nme.1434.  
URL <https://onlinelibrary.wiley.com/doi/10.1002/nme.1434>
- [4] M. Shashkov, K. Lipnikov, Remapping between meshes with isoparametric cells: a case study.
- [5] D. A. Ibanez, conformal mesh adaptation on heterogeneous supercomputers, PhD, Rensselaer Polytechnic Institute, Troy, NY (Nov. 2016).
- [6] S. R. Slattery, Mesh-free data transfer algorithms for partitioned multiphysics problems: Conservation, accuracy, and parallelism, *J. Comput. Phys.* 307 (2016) 164–188. doi:10.1016/j.jcp.2015.11.055.
- [7] M. F. Adams, M. Knepley, D. S. Finn, J. V. Puszta, A Projection Method for Particle Resampling, *Computer Physics Communications* 321 (2026). doi:10.1016/j.cpc.2026.110024.  
URL <https://www.sciencedirect.com/science/article/pii/S0010465526000068>
- [8] X. Jiao, M. T. Heath, Common-refinement-based data transfer between non-matching meshes in multiphysics simulations, *Int. J. Numer. Methods Eng.* 61 (14) (2004) 2402–2427. doi:10.1002/nme.1147.
- [9] P. Farrell, M. Piggott, C. Pain, G. Gorman, C. Wilson, Conservative interpolation between unstructured meshes via supermesh construction, *Computer Methods in Applied Mechanics and Engineering* 198 (33-36) (2009) 2632–2642. doi:10.1016/j.cma.2009.03.004.  
URL <https://linkinghub.elsevier.com/retrieve/pii/S0045782509001315>
- [10] P. E. Farrell, J. R. Maddison, Conservative interpolation between volume meshes by local galerkin projection, *Computer Methods in Applied Mechanics and Engineering* 211–212 (2011) 1171–1183.
- [11] F. Hasan, C. W. Smith, M. S. Shephard, R. M. Churchill, G. J. Wilkie, P. K. Romano, P. C. Shriwise, J. S. Merson, GPU Acceleration of Monte Carlo Tallies on Unstructured Meshes in OpenMC with PUMI-Tally,

submitted. (Apr. 2025). doi:10.48550/arXiv.2504.19048.  
URL <http://arxiv.org/abs/2504.19048>

- [12] J. S. Merson, H. Belanger, P. Singh, Spatially Continuous Functional Expansion Tallies on Unstructured Meshes, Torino, Italy, under Review.
- [13] G. Chourdakis, K. Davis, B. Rodenberg, M. Schulte, F. Simonis, B. Uekermann, G. Abrams, H.-J. Bungartz, L. Cheung Yau, I. Desai, K. Eder, R. Hertrich, F. Lindner, A. Rusch, D. Sashko, D. Schneider, A. Totounferoush, D. Volland, P. Vollmer, O. Z. Koseomur, preCICE v2: A sustainable and user-friendly coupling library, Open Research Europe 2 (2022) 51. doi:10.12688/openreseurope.14445.1.  
URL <https://open-research-europe.ec.europa.eu/articles/2-51/v1>
- [14] S. R. Slattery, P. P. H. Wilson, R. P. Pawlowski, The Data Transfer Kit: A Geometric Rendezvous-Based Tool for Multiphysics Data Transfer, American Nuclear Society, Sun Valley, ID, 2013, p. 11.
- [15] A. Novak, D. Andrs, P. Shriwise, J. Fang, H. Yuan, D. Shaver, E. Merzari, P. Romano, R. Martineau, Coupled Monte Carlo and thermal-fluid modeling of high temperature gas reactors using Cardinal, Annals of Nuclear Energy 177 (2022) 109310. doi:10.1016/j.anucene.2022.109310.  
URL <https://linkinghub.elsevier.com/retrieve/pii/S0306454922003450>
- [16] O. C. Zienkiewicz, J. Z. Zhu, The superconvergent patch recovery and a posteriori error estimates. Part 2: Error estimates and adaptivity, International Journal for Numerical Methods in Engineering 33 (7) (1992) 1365–1382. doi:10.1002/nme.1620330703.  
URL <http://doi.wiley.com/10.1002/nme.1620330703>
- [17] O. Zienkiewicz, J. Zhu, The superconvergent patch recovery (SPR) and adaptive finite element refinement, Computer Methods in Applied Mechanics and Engineering 101 (1-3) (1992) 207–224. doi:10.1016/0045-7825(92)90023-D.  
URL <http://linkinghub.elsevier.com/retrieve/pii/004578259290023D>

- [18] H.-J. Bungartz, F. Lindner, B. Gatzhammer, M. Mehl, K. Scheufele, A. Shukaev, B. Uekermann, preCICE – A fully parallel library for multi-physics surface coupling, *Computers & Fluids* 141 (2016) 250–258. doi:10.1016/j.compfluid.2016.04.003.  
URL <https://linkinghub.elsevier.com/retrieve/pii/S0045793016300974>
- [19] Z. Ding, G. Mei, S. Cuomo, N. Xu, H. Tian, Performance Evaluation of GPU-Accelerated Spatial Interpolation Using Radial Basis Functions for Building Explicit Surfaces, *International Journal of Parallel Programming* 46 (5) (2018) 963–991. doi:10.1007/s10766-017-0538-6.  
URL <https://doi.org/10.1007/s10766-017-0538-6>
- [20] D. Schneider, T. Shrader, B. Uekermann, Data-Parallel Radial-Basis Function Interpolation in preCICE, in: 10th edition of the International Conference on Computational Methods for Coupled Problems in Science and Engineering, CIMNE, 2023. doi:10.23967/c.coupled.2023.016.  
URL <https://www.scipedia.com/public/2023r>
- [21] N. Morrical, S. Zellmann, A. Sahistan, P. Shriwise, V. Pascucci, Attribute-Aware RBFs: Interactive Visualization of Time Series Particle Volumes Using RT Core Range Queries, *IEEE Transactions on Visualization and Computer Graphics* (2023) 1–11doi:10.1109/TVCG.2023.3327366.  
URL <https://ieeexplore.ieee.org/document/10296023/>
- [22] D. Hermes, P.-O. Persson, High-order Solution Transfer between Curved Triangular Meshes, *Communications in Applied Mathematics and Computational Science* 20 (1) (2025) 1–27, arXiv:1810.06806 [math]. doi:10.2140/camcos.2025.20.1.  
URL <http://arxiv.org/abs/1810.06806>
- [23] D. A. Dunavant, High degree efficient symmetrical gaussian quadrature rules for the triangle, *Int. J. Numer. Methods Eng.* 21 (1985) 1129–1148. doi:10.1002/nme.1620070316.
- [24] P. Keast, Moderate-degree tetrahedral quadrature formulas, *Computer Methods in Applied Mechanics and Engineering* 55 (3) (1986) 339–348. doi:[https://doi.org/10.1016/0045-7825\(86\)90059-9](https://doi.org/10.1016/0045-7825(86)90059-9).

URL <https://www.sciencedirect.com/science/article/pii/S0045782586900599>

- [25] X. Jiao, M. T. Heath, Overlaying surface meshes, part i: Algorithms, *International Journal of Computational Geometry & Applications* 14 (6) (2004) 379–402. doi:10.1142/S0218195904001512.
- [26] D. H. Eberly, *3D Game Engine Design: A Practical Approach to Real-Time Computer Graphics*, 2nd Edition, CRC Press, Boca Raton, 2007. doi:10.1201/b18212.
- [27] D. Powell, T. Abel, An exact general remeshing scheme applied to physically conservative voxelization, *Journal of Computational Physics* 297 (2015) 340–356. doi:<https://doi.org/10.1016/j.jcp.2015.05.022>.  
URL <https://www.sciencedirect.com/science/article/pii/S0021999115003563>
- [28] D. Powell, R3d: Software for fast, robust geometric operations in 3d and 2d, Tech. Rep. LA-UR-15-26964 (Aug. 2015).
- [29] R. Osada, T. Funkhouser, B. Chazelle, D. Dobkin, Shape distributions, *ACM Transactions on Graphics (TOG)* 21 (4) (2002) 807–832. doi:10.1145/571647.571648.
- [30] M. H. Kalos, P. A. Whitlock, *Monte Carlo Methods*, 2nd Edition, Wiley-VCH Verlag GmbH & Co. KGaA, Weinheim, Germany, 2008, online ISBN: 9783527626212. doi:10.1002/9783527626212.
- [31] J. S. Merson, C. W. Smith, M. S. Shephard, F. Hasan, A. Paudel, A. Castillo-Crooke, J. Mathew, M. Elahi, PCMS: Parallel Coupler for Multimodel Simulations, arXiv preprint arXiv:2510.18838 Submitted on 21 Oct 2025 (Oct. 2025). arXiv:2510.18838, doi:10.48550/arXiv.2510.18838.  
URL <https://arxiv.org/abs/2510.18838>
- [32] C. Geuzaine, J.-F. Remacle, Gmsh: A three-dimensional finite element mesh generator with built-in pre- and post-processing facilities, *International Journal for Numerical Methods in Engineering* 79 (11) (2009) 1309–1331. doi:10.1002/nme.2579.